energies

MDPI

Article

Numerical Investigations of a Counter-Current Moving Bed Reactor for Thermochemical Energy Storage at High Temperatures

Nicole Carina Preisner [1,*], Inga Bürger [2], Michael Wokon [1] and Marc Linder [2]

[1] Institute of Engineering Thermodynamics, DLR, Linder Höhe, 51147 Köln, Germany
[2] Institute of Engineering Thermodynamics, DLR, Pfaffenwaldring 38-40, 70569 Stuttgart, Germany
* Correspondence: nicole.preisner@dlr.de

Received: 27 January 2020; Accepted: 5 February 2020; Published: 10 February 2020

Abstract: High temperature storage is a key factor for compensating the fluctuating energy supply of solar thermal power plants, and thus enables renewable base load power. In thermochemical energy storage, the thermal energy is stored as the reaction enthalpy of a chemically reversible gas-solid reaction. Metal oxides are suitable candidates for thermochemical energy storage for solar thermal power plants, due to their high reaction temperatures and use of oxygen as a gaseous reaction partner. However, it is crucial to extract both sensible and thermochemical energy at these elevated temperatures to boost the overall system efficiency. Therefore, this study focuses on the combined extraction of thermochemical and sensible energy from a metal oxide and its effects on thermal power and energy density during discharging. A counter-current moving bed, based on manganese-iron-oxide, was investigated with a transient, one-dimensional model using the finite element method. A nearly isothermal temperature distribution along the bed height was formed, as long as the gas flow did not exceed a tipping point. A maximal energy density of 933 kJ/kg was achieved, when $(Mn,Fe)_3O_4$ was oxidized and cooled from 1050 °C to 300 °C. However, reaction kinetics can limit the thermal power and energy density. To avoid this drawback, a moving bed reactor based on the investigated manganese-iron oxide should combine direct and indirect heat transfer to overcome kinetic limitations.

Keywords: moving bed; thermochemical energy storage; redox reaction

1. Introduction

High temperature thermal energy storage is one key factor for further proliferation of concentrated solar power (CSP) plants. The integration allows a plant to decouple energy supply from energy demand, e.g., for cloudy days or during the night. Thus, CSP coupled with thermal energy storage is able to provide base load electricity, making it a renewable alternative for fossil fuel power plants. Thermochemical energy storage is a promising option for thermal energy storage, next to latent or sensible energy storage. In this concept the reaction enthalpy of a reversible gas-solid reaction is utilized as thermal energy storage, which potentially enables loss-free energy storage in the form of the separated products and offers the advantage of high energy densities [1,2]. The endothermic reaction (charging phase) can be driven by concentrated solar thermal energy, while the exothermic reaction (discharging phase) recovers the stored thermochemical energy during hours of high energy demand or low solar irradiation. Usually, the separate storage of gas and solid for thermochemical energy storage systems involves complex gas handling, e.g., for the CaO/CO_2 or CaO/H_2O reaction systems. In contrast, metal oxides react with oxygen under atmospheric pressure. Oxygen as a gaseous reaction partner drastically simplifies the system's complexity, because ambient air can act as reactive gas.

Therefore, no separate storage of the gas is needed and an open reactor system is feasible, which makes metal oxides suitable thermal energy storage material for CSP plants [3,4]. Furthermore, the utilization of metal-oxide particles as heat transfer medium and storage material is possible. The investigated system concept based on metal-oxide particles is shown in Figure 1.

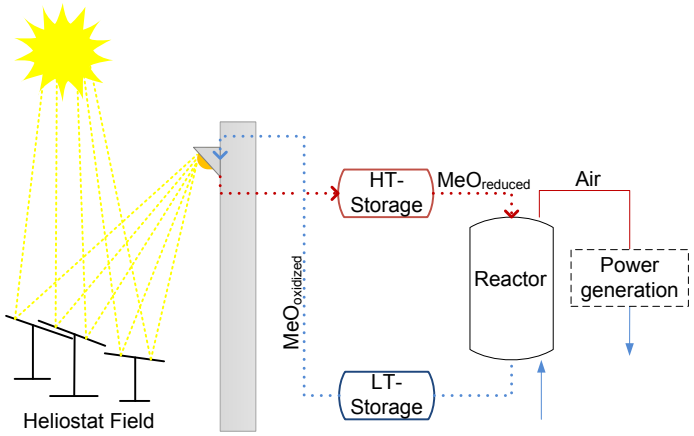

Figure 1. Concept of thermochemical energy storage based on metal oxide particles for solar tower applications. The metal oxide particles are cycled between a solar tower, high temperature (HT) storage, the reactor for discharging, and a low temperature (LT) storage.

Metal oxide particles are circulated between a solar receiver for charging and a continuously operated reactor for discharging. At this point, it is crucial to extract the thermochemical and sensible share in stored thermal energy to boost the overall system efficiency, since metal oxides react under elevated temperatures (700 °C to 1400 °C [3,4]). The considered system concept is able to supply dispatchable renewable energy. Furthermore, the storage capacity and system power are decoupled, which results in an improved operational flexibility.

This work focuses, therefore, on manganese-iron oxide as a reference material to investigate the simultaneous sensible and thermochemical heat extraction. The reaction equation of the redox reaction of manganese-iron oxide is given below:

$$6\,(\mathrm{Mn,Fe})_2\mathrm{O}_3 + \Delta_R\,\mathrm{H} \rightleftharpoons 4\,(\mathrm{Mn,Fe})_3\mathrm{O}_4 + \mathrm{O}_2. \quad (1)$$

The $(\mathrm{Mn,Fe})_2\mathrm{O}_3$ granules with a Mn/(Mn + Fe) ratio of 0.75 were already successfully tested in a lab-scale packed bed reactor by our group [5]. Moreover, sufficient redox cycle stability of manganese-iron oxide has been proven by Wokon et al. [6], which represents a part of our preliminary work for this study.

In the presented system (Figure 1), the discharging is realized using a moving bed reactor for direct heat transfer to a counter-current gas flow. The moving bed concept is widely applied when the redox reaction of metal oxides is in focus; e.g., in chemical-looping combustion (CLC) or for iron-ore reduction in the steel-making industry. In general, a moving bed reactor presents a simple design for continuous movement of particles with the possibility to transfer sensible and thermochemical energy from the particles to a gas flow [7]. In CLC, high reaction conversion of metal oxide particles has been reported for moving bed reactors in bench-scale [8], with a thermal power of 25 kW [9] or up to 30 kW [7]. Furthermore, the moving bed design causes low mechanical stress for the particles and low parasitic losses. Therefore, the concept of a moving bed reactor was chosen for this study.

Several steady-state models have been suggested for a moving bed simulation. A one-dimensional (1D), steady-state model with an assumed local thermal equilibrium is presented for iron making in [10] and validated with a lab-scale reactor. Optimal operational parameters for iron making using a counter-current moving bed, i.e., a shaft furnace, are obtained with a 1D steady-state model in [11–13], where no local thermal equilibrium between gas and solid is assumed. The authors of [14] set up a 1D

model for the direct reduction of hematite in a moving bed in dimensionless form. The reaction in a pellet is simulated with a three-moving-front model and the inclusion of the water-gas shift reaction is discussed. Furthermore, a 2D model was developed, including a shrinking core model [15] for the kinetics of iron oxide reduction.

Transient models have been proposed as well for both CLC and iron-making processes. The authors of [16] developed a 1D model for the direct reduction of hematite in a counter-current moving bed reactor. A modified grain model is applied for the kinetics of the multiple gas-solid reactions in the pellet and was validated with experimental data. In [17], a 1D model for direct and indirect heat transfer in a counter-current moving bed equipped with heat transfer tubes is proposed for post combustion CO_2 capture. The effect of the flow rate on CO_2 capture is discussed, as is a dynamic process response to variations of inlet temperature, solid sorbent loading, and gas composition.

So far, simulative approaches on moving bed reactors, based on the redox reaction of metal oxides, focus mainly on the overall conversion; i.e., the conversion of fuel or oxygen carrier in chemical-looping combustion or the production of iron in the steel-making industry. However, the envisaged system concept (see Figure 1) relies on a counter-current moving bed reactor, which is optimized for gas-solid heat transfer, including both thermochemical and sensible thermal energy. As a consequence, this study focuses on the extraction of thermal energy and the effect of the conversion and operational parameters on achievable thermal power and energy density. Furthermore, the combined extraction of thermochemical and sensible thermal energy is discussed with respect to power and energy density. A transient 1D model is presented for a counter-current moving bed based on the oxidation of $(Mn_{0.75}Fe_{0.25})_3O_4$ applied as reference material. The model is validated with experimental data of a fixed-bed reactor. The limiting factors of the moving bed concept, in the context of thermochemical energy storage, are investigated further by means of sensitivity analyses.

2. Model Description

This work presents a one-dimensional FEM model of a counter-current moving bed reactor, suitable for thermal energy extraction in the presented system (Figure 1). At first, the geometry is described and assumptions are stated. Then, governing equations are presented and initial and boundary conditions are given.

2.1. Geometry of the Moving Bed

The 1D geometry of the counter-current moving bed reactor is presented in Figure 2a. A bed height of 0.7 m is simulated with the gas inlet at position $x = 0$ m and the particle inlet at $x = 0.7$ m. A mesh refinement study showed that as the number of elements in mesh increased from 100 to 1000 and from 1000 to 2000, the solid outlet temperature changed by 1.2 % and 0.016 ‰ respectively. Since the results do not change much by increasing the number of elements beyond 1000, the geometry is represented by 1000 elements of equal size.

2.2. Assumptions

The following assumptions are made:

(i) The characteristic behavior of a counter-current moving bed reactor can be represented by a 1D model, since the main effects are expected to occur in the axial direction. Thus, the thermal energy losses to the surrounding are neglected.
(ii) For the gaseous components of air, the ideal gas law can be applied.
(iii) The total porosity of the manganese-iron oxide bulk does not change between oxidized and reduced phase or over consecutive cycles, based on [18] for a similar material composition.
(iv) The solid particles have a homogeneous temperature distribution and are treated as a continuum, since the Biot-number is sufficiently small.

(v) The work done by pressure change can be neglected in the energy balance for the gas phase, based on ([19] p. 41).

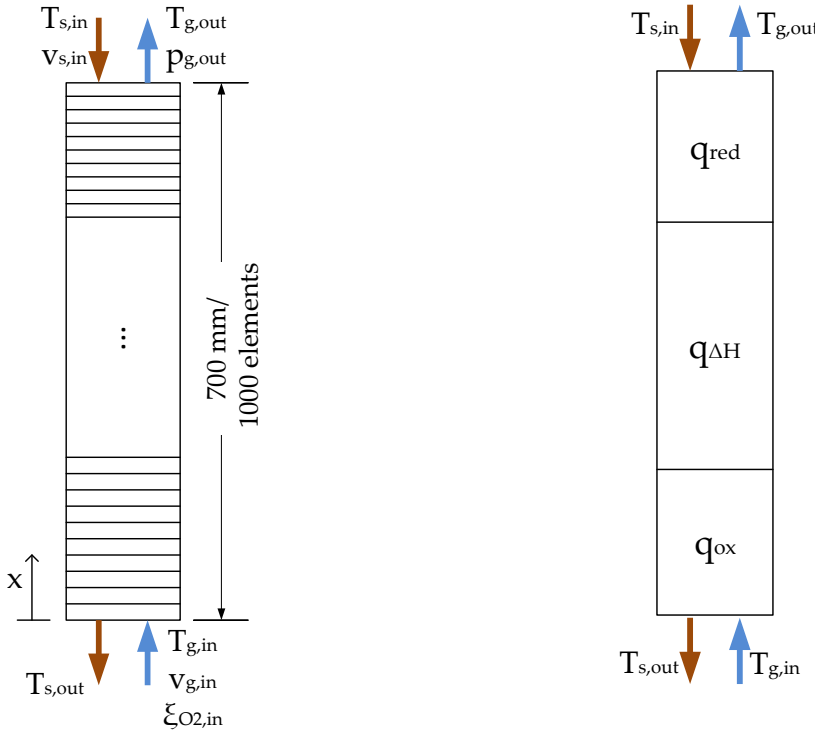

(**a**) (**b**)

Figure 2. (**a**) 1D geometry of the moving bed reactor, including the boundary conditions at the inlet (in) or outlet (out) of the gas (g) and solid (s) flows. (**b**) Schematic description of the three heat transfer sections: sensible thermal energy of the reduced phase (q_{red}), thermochemical energy due to reaction enthalpy ($q_{\Delta H}$), and sensible thermal energy of the oxidized phase (q_{ox}).

2.3. Mathematical Formulation

The governing equations are derived as follows, considering the assumptions and simplifications. The mass balance for the gas phase is expressed as:

$$\frac{\partial(\epsilon\rho_g)}{\partial t} + \nabla \cdot (\rho_g \vec{v}_g) = -(1-\epsilon)q_R, \tag{2}$$

where ϵ is the total void fraction in the bulk, ρ_g the gas density, $\vec{v}_g$ the superficial gas velocity, and q_R the chemical production rate.

As the O_2 concentration changes due to the reaction, and the reaction rate depends on the O_2 partial pressure, the mass balance of O_2 also needs to be considered. The mass balance for O_2 is:

$$\epsilon\rho_g \frac{\partial \xi_{O_2}}{\partial t} + \rho_g \vec{v}_g \cdot \nabla \xi_{O_2} - \nabla \cdot (\rho_g D \nabla \xi_{O_2}) = -(1-\epsilon)(1-\xi_{O_2})q_R, \tag{3}$$

where ξ_{O_2} is the mass fraction of O_2, and D the diffusion coefficient between O_2 and N_2.

The momentum equation for the gas phase is considered according to Darcy's law, where the superficial gas velocity $\vec{v}_g$ and the pressure difference ∇P are correlated:

$$\vec{v}_g = -\frac{K}{\mu}\nabla P. \tag{4}$$

Here, μ is the dynamic viscosity of the gas. The permeability constant K is determined with the Carman-Kozeny relationship $K = \frac{d_p^2 \epsilon_b^3}{180(1-\epsilon_b)^2}$, which is valid for approximately spherical shaped particles with a narrow range of diameters d_p. In this case, ϵ_b is the bulk porosity and ϵ_{por} the particle porosity, which are linked to the total porosity ϵ according to:

$$(1-\epsilon) = (1-\epsilon_b)(1-\epsilon_{por}). \tag{5}$$

The energy balance of the gas phase and solid phase can be written according to ([19] p. 42):

$$\left(\epsilon \rho_g c_{p_g}\right) \frac{\partial T_g}{\partial t} + \left(\rho_g c_{p_g} \vec{v}_g\right) \cdot \nabla T_g = -\nabla \cdot \left(-\epsilon_b \lambda_g \nabla T_g\right) + h_{gs} a_{gs} (T_s - T_g), \tag{6}$$

$$((1-\epsilon)\rho_s c_s) \frac{\partial T_s}{\partial t} + (\rho_s c_s \vec{v}_s) \cdot \nabla T_s = -\nabla \cdot \left(-\lambda_{s,eff} \nabla T_s\right) + h_{gs} a_{gs} (T_g - T_s) + (1-\epsilon) q_R \Delta H. \tag{7}$$

Here, ρ_g and ρ_s are the density; c_{p_g} and c_s are the specific heat capacities; T_g and T_s are the temperatures; and $\vec{v}_g$ and $\vec{v}_s$ are the superficial velocities of the gas and solid phases, respectively. The effective thermal conductivity of the solid $\lambda_{s,eff} = \lambda_{bulk,eff} - \epsilon_b * \lambda_g$ is calculated with the effective thermal conductivity of the bulk $\lambda_{bulk,eff}$ according to the extended Zehner-Bauer-Schlünder model, which also includes the radiative contribution [20,21]. For the convective heat transfer coefficient h_{gs} in a counter-current moving bed reactor, the correlation according to [22] is applied, together with the specific surface area $a_{gs} = \frac{6(1-\epsilon_b)}{d_p}$.

Initial and Boundary Conditions

The initial temperatures of gas and solid are set to 1050 °C. At the gas inlet ($x = 0$ m), the mass fraction of O_2 $\xi_{O_2,in}$ is set to 23.27%, and the gas inlet temperature $T_{g,in}$ equals 300 °C. Similarly, for the particle inlet ($x = 0.7$ m), the gas pressure $p_{g,out}$ is set to ambient conditions (1013.25 hPa), and the particle inlet temperature $T_{s,in}$ to 1050 °C.

3. Material Properties

The considered material $(Mn_{0.75}Fe_{0.25})_2O_3$ was investigated concerning thermodynamics and kinetics in a previous study [6] of our group. The particles were produced by VITO (Mol, Belgium) via build-up granulation. For the preparation, the raw materials Mn_3O_4 (Trimanox electronic grade, Chemalloy) and Fe_2O_3 (98% metal basis, Alfa Aesar) were mixed in powder form, before the granulation using an Eirich Mixer (see [6] for further details). Table 1 presents a compilation of relevant material properties for the model description.

Three main parameters of the material are characteristic for the planned combination of heat transfer of thermochemical and sensible energy (see Figure 2b). Firstly, the heat transfer of sensible energy (q_{red}) between the reduced solid phase and the gas flow is confined downwards by the onset temperature of the oxidation, because this temperature is regarded as the lower threshold value of this heat transfer section. Due to the occurrence of thermal hysteresis of the manganese-iron oxide, the temperature threshold value for the oxidation onset determined via simultaneous thermal analyses deviates from the calculated thermodynamic equilibrium temperature. For example, an oxygen partial pressure of 20.4 kPa yields an oxidation onset temperature of 918.3 °C, whereas thermodynamic equilibrium calculations result in 966.8 °C [6]. Secondly, the transfer of the released heat of reaction ($q_{\Delta H}$) is directly influenced by the reaction kinetics of the Mn-Fe oxide. The oxidation kinetics has been already determined by means of thermogravimetric analysis [6]:

$$\frac{\mathrm{d}\alpha}{\mathrm{d}t} = 1.78 \times 10^{16} \frac{1}{s} \cdot \exp\left(-\frac{463.53\ \frac{\mathrm{kJ}}{\mathrm{mol}}}{R \cdot T}\right) \cdot \left(ln\frac{p_{\mathrm{O}_2}}{p_{eq}(T)}\right)^{7.06} \times 1.38(1-\alpha)(-ln(1-\alpha))^{1-\frac{1}{1.38}}. \quad (8)$$

Table 1. Material parameters.

Parameter	Symbol	Value/Correlation	Unit	Reference
Mean particle diameter	d_p	2.42	mm	[6]
Bulk density	ρ_{bulk}	1353	kg/m^3	[5]
Reaction enthalpy, based on oxidized phase	$\Delta_r H$	271	J/g	[6]
Specific heat capacity of Mn_3O_4	$c_{p_{red}}$	$\left(613.07996 + 2.58034(\frac{T_s}{\mathrm{K}} - 298)^{0.68764}\right)$	J/kg/K	[23]
Specific heat capacity of $(Mn_{0.75}Fe_{0.25})_2O_3$	$c_{p_{ox}}$	$\left(669.28596 + 0.62604(\frac{T_s}{\mathrm{K}} - 298)^{0.8982}\right)$	J/kg/K	see Appendix A
Intrinsic thermal conductivity for Mn_2O_3 (400 K to 1400 K)	λ_s	$0.99395 + 6.98315 \times 10^{-4} \cdot \frac{T_s}{\mathrm{K}}$ $-1.23972 \times 10^{-7} \cdot \frac{T_s^2}{\mathrm{K}}$	W/m/K	polynomial fit based on c_p for Mn_2O_3 [23] and thermal diffusivity [24]
True density of $(Mn_{0.75}Fe_{0.25})_2O_3$	ρ_s	5125	kg/m^3	measured via He-pycnometry
Total porosity	ϵ	0.736	–	calculated with true density
Bulk porosity	ϵ_b	0.34	–	calculated with Equation (5)
Intra-particle porosity	ϵ_{por}	0.6	–	measured via Hg-intrusion-porosimetry

Finally, the specific heat capacity $c_{p_{ox}}$ is a crucial thermophysical parameter considering the amount of heat that can be transferred between the oxidized phase and the gas flow (q_{ox}). The $c_{p_{ox}}$ values of the phase $(Mn_{0.75}Fe_{0.25})_2O_3$ were determined by means of differential scanning calorimetry (DSC). The specific heat capacity of the reduced phase $c_{p_{red}}$ is approximated with the specific heat capacity of Mn_3O_4 [23]. Values applied for $c_{p_{ox}}$ and $c_{p_{red}}$ are illustrated in Appendix A.

The thermal conductivity of the specific oxide $(Mn_{0.75}Fe_{0.25})_2O_3$ is unavailable presently. Therefore, the reported values for manganese oxides are applied for determination of the intrinsic thermal conductivity of the solid material λ_s. With the specific heat capacity of Mn_2O_3 [23] and thermal diffusivity [24] of manganese ores, the intrinsic thermal conductivity is estimated for a temperature range between 400 K and 1400 K. A polynomial fit function for this temperature range (listed in Table 1) is used as an input value for the determination of the effective thermal conductivity of the bulk $\lambda_{bulk,eff}$ according to the extended Zehner-Bauer-Schlünder model [20,21]. Furthermore, the emissivity of the manganese-iron oxide particles was approximated to 0.87, based on measured values for Fe_2O_3 particles [25] and a Mn-Fe-Zr-coating [26].

4. Validation

The model is validated with experimental results from our group [5] using a fixed bed reactor for direct heat transfer between $(Mn_{0.75}Fe_{0.25})_2O_3/(Mn_{0.75}Fe_{0.25})_3O_4$ and a gas flow of ambient air.

4.1. Experimental Setup for Validation

This section presents only the data of the experimental setup relevant for the model validation. A detailed description of the schematic setup and further experimental investigations can be found in [5]. A lab-scale tube reactor (nickel-based alloy 2.4856) with an inner diameter of 54.3 mm is filled

with 471.2 g metal-oxide particles $(Mn_{0.75}Fe_{0.25})_2O_3$. Air heated by means of an electrical gas heater, integrated into the reactor unit, enters the reaction bed from the bottom via a perforated plate and a gas distribution disc. A vertical tube furnace encases the reactor tube to assist the gas heater, minimize heat losses to the ambient, and to control the bulk temperature. Four thermocouples (Type K, class 1, $\varnothing = 1$ mm) measure the temperature profile in the central position along the bed height at distances of 10 mm (T1), 50 mm (T2), 90 mm (T3), and 130 mm (T4) from the gas distribution disc. The oxygen concentration in the off-gas is analyzed via a paramagnetic oxygen measurement (NGA-2000 MLT-2, Emerson Process Management/Rosemount Analytical). A change of the oxygen concentration in the off-gas can be attributed to the redox reaction of the metal-oxide bulk and is thus used for conversion calculations.

4.2. Model Validation

The model is validated based on a discharging experiment in the fixed bed reactor using the described granular manganese-iron oxide particles. Ten redox cycles have been performed with the material prior to this dynamic discharging step presented here. The validation experiment corresponds to the experiment cycle number 11 in [5]. In the preceding charging stage, the bulk was heated to a temperature of 1040 °C ($T_{s,0}$) and reduced with 10 L/min air flow $\dot{V}_n$. All gas flow rates in this study are based on norm conditions ($T_{g,n} = 0$ °C and $p_n = 1013.25$ hPa). For discharging, the tube furnace and the air inlet temperature ($T_{g,in}$) were reduced at a rate of 5 K/min down to 400 °C, during which phase the oxidation was initiated. In Figure 3 simulative and experimental results are displayed.

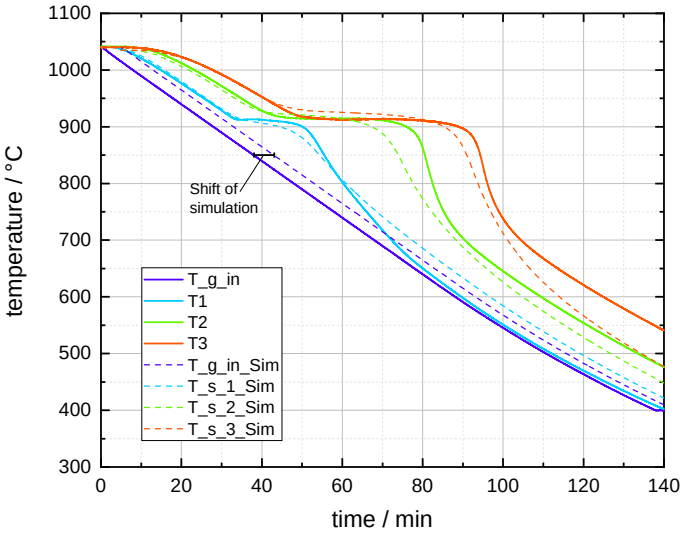

Figure 3. Simulation of dynamic cooling with oxidation of $(Mn_{0.75}Fe_{0.25})_3O_4$ in a lab-scale fixed bed reactor. Solid lines display temperatures measured in the experiment, whereas dashed lines present the simulated temperatures. The simulation was shifted by 5 min to allow for a better comparison.

The solid temperatures decrease until the exothermic oxidation stabilizes the temperatures at a plateau for about 16 min at a bed height of 10 mm (T1) and up to 38 min at a bed height of 90 mm (T3). The simulated solid temperatures show a similar trend with a maximal offset of 13 °C to the measured temperature plateau of ≈913 °C. However, during the first minutes of the discharging phase, the difference between the gas inlet temperature and the solid temperature T1 in the experiment exceeds the difference in the simulation. To compensate the experimental delay, the gas inlet temperature is shifted by 5 min for the simulation. A detailed discussion of this time shift is presented in Appendix B. In the end, the model sufficiently reflects the oxidation progress and the cooling effect of the gas on the

manganese-iron oxide. The simulation meets the onset temperature of the reaction and is able to describe the course of the solid temperature in the temperature range, where only thermal energy is transferred.

5. Results and Discussion

As a next step, the bulk movement is included in the model, which is based on the same equations (Section 2.3). This model is applied to investigate the impacts of operational parameters, i.e., gas and particle flow, on the thermal power and energy density.

5.1. Moving Bed Design

At first, a rough estimate for such a counter-current moving bed system has to be made, since now the power output is affected by further operational parameters, in comparison to a fixed-bed reactor. As an exemplary system, a thermal power of 3 kW is considered as realistic, which is in range of the discussed fixed-bed reactor. Therefore, the operational parameters required as starting values for the moving bed simulation were analytically determined for a thermal power of 3 kW. For this initial estimation of particle and gas mass flows and required bed height, only convective heat transfer between gas and solid is considered. Since a heat transfer of sensible and thermochemical energy between metal oxide particles and a counter-current gas stream occurs, the moving bed can be divided into three sections (see also, Figure 2b):

1. Sensible heat transfer q_{red} till metal oxide granules reach the onset temperature of oxidation ($\dot{Q}_{red} = \int_{T_{s,in}}^{T_{s,out}} \dot{m}_s c_{p,s}(T_s)\,\mathrm{d}T_s$);
2. Heat transfer of thermochemical energy $q_{\Delta H}$, where metal oxide granules are oxidized and the released reaction enthalpy is transferred to the gas stream ($q_{\Delta H} = \Delta_r H$);
3. Sensible heat transfer q_{ox} till metal oxide granules reach the desired particle outlet temperature ($\dot{Q}_{ox} = \int_{T_{g,in}}^{T_{g,out}} \dot{m}_g c_{p,g}(T)\,\mathrm{d}T_g$).

The estimation of mass flows is based on the NTU (number of transfer units) method, which was developed for sensible heat exchangers. One crucial characteristic factor to evaluate a moving bed reactor is the heat capacity rate ratio F, defined as:

$$F = \frac{\dot{m}_{red} \cdot \tilde{c}_{p,red}(T_{m,red}) + \dot{m}_{ox} \cdot \tilde{c}_{p,ox}(T_{m,ox})}{\dot{m}_g \cdot \tilde{c}_{p,g}(T_{m,g})}. \tag{9}$$

Here, $\dot{m}_{red}$ and $\dot{m}_{ox}$ are the mass flow rates, and $\tilde{c}_{p,red}$ and $\tilde{c}_{p,ox}$ are the averaged specific heat capacities for the mean temperature $T_{m,red}$ and $T_{m,ox}$ of the reduced and oxidized phase, respectively. The rough estimation yields that a particle mass flow of 4 g/s in counter-current to a gas flow $\dot{V}_n$ of 183 L/min is necessary to achieve a heat transfer of 3 kW, considering also the boundary conditions given in Section 2.3. The gas and solid velocities v_g and v_s are calculated with an assumed reactor diameter of 0.152 m. A detailed description for the calculations is given in Appendix C.

5.2. Temperature Profiles of a Thermochemical Moving Bed

The estimated gas and particle flow rates were used as initial input values for first simulations. Figure 4 displays the solid temperature along the height of the moving bed for time steps normalized to $t_{stat} = 400$ min, which equals the time till a stationary temperature profile is achieved for the given particle and gas flow rates. The particle bed is simulated with a starting and inlet temperature of 1050 °C and a gas inlet temperature of 300 °C. Therefore, the particle temperature starts to decrease at position 0. The highest temperature gradient arises between the gas inlet and 5 cm above. A nearly isothermal temperature zone in the range of 900 °C to 942 °C moves upwards until a steady state is reached. After 400 min, the particles exit the moving bed with 329 °C at position $x = 0$, and a steady-state operation is reached.

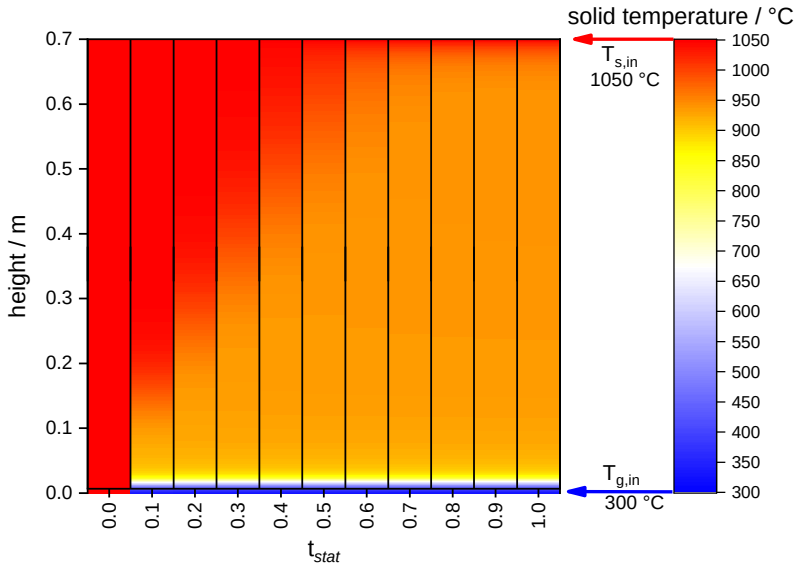

Figure 4. Heat map for the solid temperature development along the bed height of 0.7 m of a moving bed with Mn-Fe-oxide particles moving with 4 g/s in counter-current to 183 L/min air flow $\dot{V}_n$. The time steps are normalized to the time t_{stat} when a stationary temperature profile occurs after 400 min for the current particle and gas flow rates.

Comparison of Inert and Thermochemical Moving Bed

The reaction was disabled for one simulation to highlight the difference between a purely sensible (inert) and a thermochemical material in a moving bed reactor. In Figure 5a two different stationary temperature profiles for the manganese-iron-oxide particles and the counter-current gas flow are displayed along the height of the moving bed.

In general, the gas and solid temperature profiles are very similar in the reactive and inert cases. Considering the reactive case, the uniform coloring in the heat map of Figure 4 ($t_{stat} = 1.0$) corresponds to the temperature plateau of the reactive case in Figure 5a. The solid temperature reaches 928 °C at a bed height of 0.1 m, and up to 940 °C at a height of 0.6 m.

Technically relevant p_{O2}-T conditions experimentally determined based on simultaneous thermal analyses (see [6]) give a temperature threshold value of 919.6 °C for the oxidation onset at a p_{O2} of 20.9 kPa. However, the equilibrium temperature for the phase change from the two-phase region "bixbyite + spinel" (spinel being the reduced phase) to the bixbyite (being the oxidized phase) was calculated to 967.9 °C for a p_{O2} of 20.9 kPa [6]. Thus, the formed temperature plateau is in between the extrapolated onset temperature and thermodynamic equilibrium of the phase boundary "bixbyite"–"bixbyite + spinel." Kinetic investigations further revealed the extremely low reaction rates of the oxidation at temperatures between the extrapolated onset temperature and the calculated equilibrium temperature [6]. In this area of "thermal hysteresis" especially, the oxidation reaction takes a long time to initiate and proceed; e.g., an isothermal oxidation at 926.6 °C required an induction period of over 30 min at an oxygen partial pressure of 20.4 kPa [6]. In Figure 5b the oxidation conversion along the bed height is displayed for an operation in steady state and corresponds to the gas and solid temperature course of the reactive case depicted in Figure 5a. The largest part of the reaction conversion is achieved in the cooling section close to the gas inlet within the first 5 cm of the bed, as the highest reaction rates occur in this temperature range of the prevailing temperature profile. However, the cooling rate seems to impede full oxidation conversion, as the conversion adds up to only 65% at the particle outlet. Remarkably, the overall conversion benefits only to a very small extent (conversion below ~0.1%) from a bed height of 60 cm, between 0.1 m and 0.7 m. In this area of nearly isothermal conditions only a small amount of heat can be transferred from solid to gas, since the gas has already

reached the effective onset temperature. However, the low conversion of the material in the nearly isothermal bed section is still sufficient to stabilize the solid temperature against the cooling effect of the gas flow and thus form the isothermal bed section. Eventually, the reactor could be shortened to a bed height of around 15 cm, without negatively influencing the conversion, thermal power, or achievable energy density for these operational parameters. However, the displayed gas and solid temperature profiles strongly depend on kinetics and the convective heat transfer coefficient. The effect of faster kinetics and lower convective heat transfer between gas and solid will be further discussed in Section 5.4.

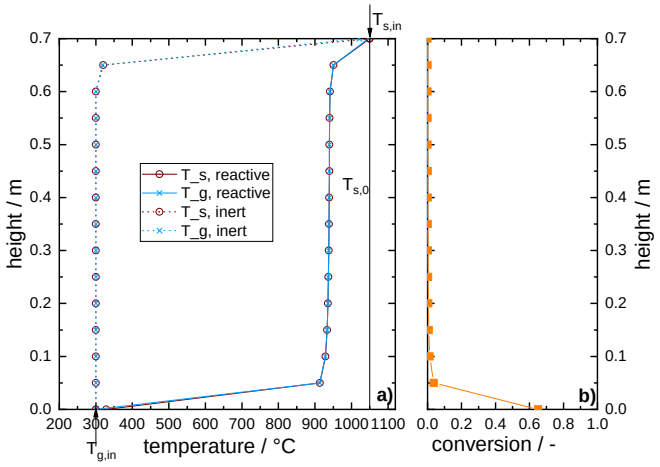

Figure 5. Results for a moving bed with 4 g/s Mn-Fe-oxide particles and counter-current air flow $\dot{V}_n$ of 183 L/min operated in steady state. (**a**) Comparison of gas and solid temperature profiles with (solid line) and without (dotted line) reaction. (**b**) Reaction conversion along the bed height for operation in steady state.

In the considered inert moving bed (Figure 5), the solid particle temperature decreases to the level of the gas inlet temperature in a distance of less than 10 cm away from the particle inlet. Thus, the bed height could be limited to the area exhibiting this large temperature gradient without loosing thermal power. Apparently, the heat flow due to the proceeding chemical reaction leads to an additional rate of heat flow from the solid to the gas compared to the case of purely sensible storage material, which shifts the major temperature gradient from the particle inlet (inert storage material) to the gas inlet (thermochemical storage material).

5.3. Flexibility of Power and Energy Density

5.3.1. The Effect of the Variation of Gas Flow Rates

In the scope of thermochemical energy storage, the main task of the simulated moving bed reactor is to transfer heat from Mn-Fe-oxide particles to a counter-current gas flow. Therefore, the effect of gas flow variation on the reactor performance is investigated in this section. In Figure 6, stationary solid temperature profiles are displayed for a particle flow rate of 4 g/s and various gas flow rates, ranging from 150 L/min to 230 L/min.

The profiles indicate a temperature plateau formation for gas flow rates between 150 L/min and 190 L/min. For higher flow rates, 210 L/min and above, a temperature profile similar to the purely inert moving bed in in Figure 5a is obtained. In this case all three sections (q_{red}, $q_{\Delta H}$, q_{ox}), described above, are present within the top 5 cm of the moving bed. The point where the stationary temperature profile and hence the storage operation changes, between 190 L/min and 210 L/min, is called the "tipping point" hereinafter. The closer the gas flow is to this tipping point, the higher the temperature gradient is below and above the temperature plateau. This fact can be attributed to the higher heat capacity flow of the gas. Furthermore, with lower gas flow rates, the particles exit the moving bed with a higher outlet temperature. The corresponding conversion of the Mn-Fe-oxide particles is depicted in

Figure 6b. For gas flow rates above the tipping point, the kinetic limitation of the material leads to a reduced conversion as a consequence of increased cooling rates. Furthermore, the particles oxidize shortly after the particle inlet; i.e., in less than 5 cm. The oxidation of the particles can only take place within the range of the topmost 5 cm below the particle inlet.

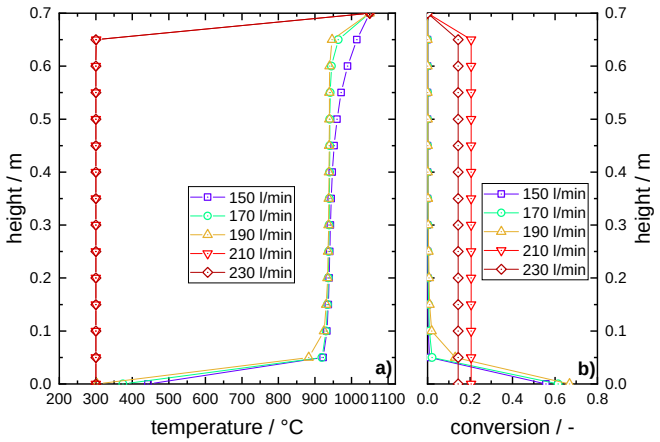

Figure 6. (**a**) Temperature profile of solid particles along the bed height of a moving bed (4 g/s particle flow rate) with different gas flow rates operated in steady state. (**b**) Conversion profiles along the bed height of the moving bed reactor operated in steady state.

The achieved conversion at the particle outlet (x = 0 m) and gas temperature at the gas outlet (x = 0.7 m) are displayed in Figure 7 in comparison to a purely inert moving bed of Mn-Fe-oxide particles with 4 g/s solid mass flow.

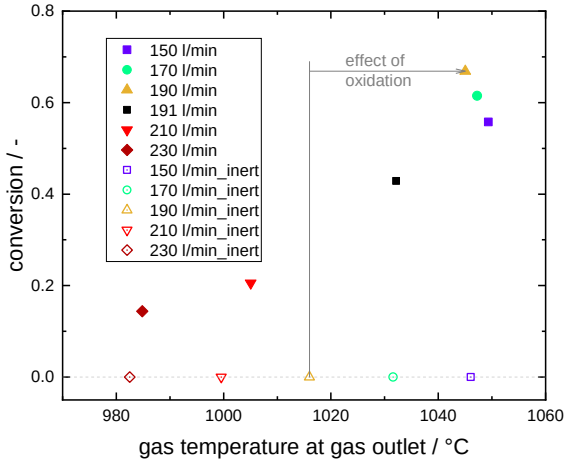

Figure 7. Obtained conversion at particle outlet (x = 0 m) and gas temperature at particle inlet (x = 0.7 m) of a moving bed (4 g/s particle flow rate) with different gas flow rates. Full symbols represent thermochemical storage material undergoing a chemical reaction; empty symbols represent inert storage material used for sensible storage only.

In general, higher gas flow rates lower the achievable gas outlet temperature. However, the increase in conversion (between $\dot{V}_n$ 210 L/min and 190 L/min) is directly correlated to a strong increase in gas outlet temperature. Changing the gas flow $\dot{V}_n$ from 190 L/min to 191 L/min shifts the gradient of the particle temperature to the particle inlet, resulting in a temperature profile similar to the profile of higher gas flow rates. This low increase of gas flow rate has a high impact on the achievable conversion and gas outlet temperature, which indicates the position of the tipping point in between those two gas flow rates for a particle flow rate of 4 g/s. A comparison to an inert moving

bed (see empty symbols at conversion 0.0 in Figure 7) highlights the benefit of the thermochemical material. In case of a gas flow $\dot{V}_n$ of 190 L/min, the gas outlet temperature is increased by 29 °C due to the additional release of the reaction enthalpy with a reaction conversion of 66.9%. However, it has to be noted that by lowering the gas flow rate to, e.g., 150 L/min, the gas outlet temperature in the inert moving bed can reach a similar level to that with reactive material.

The correlation of transferred thermal power in a moving bed reactor with 4 g/s of Mn-Fe-oxide particles to the energy density is displayed for various gas flow rates in Figure 8.

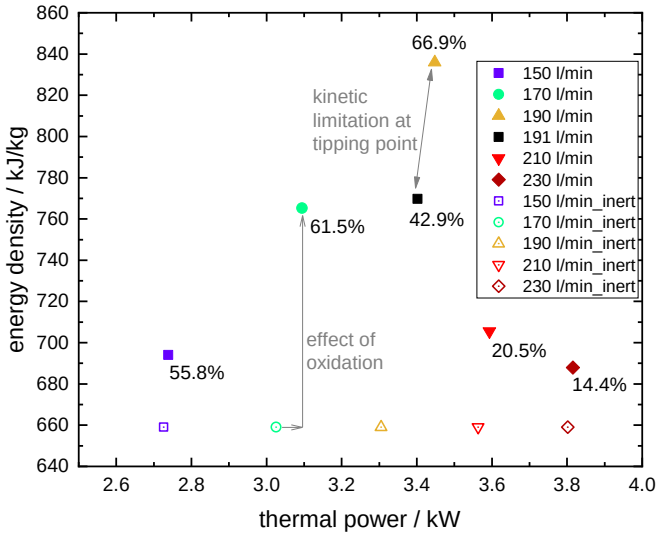

Figure 8. Thermal power and energy density of a moving bed of 4 g/s with different gas flow rates $\dot{V}_n$. The numbers next to the full symbols represent the conversion (%) achieved in steady state operation. Empty symbols represent the Mn-Fe-oxide particles acting only as sensible thermal storage material.

The calculation of the resulting gravimetric energy density is based on the solid inlet and outlet temperature, the specific heat capacity as stated in Table 1, and the achieved conversion of the Mn-Fe oxide (as highlighted in Figure 8). For the determination of the transferred thermal power, the corresponding rise in gas temperature is considered. Figure 8 also illustrates the results for a purely inert moving bed under the same operational conditions. In the investigated range of gas flow rates, the thermal power generally increases with increasing flow rate, whereas the energy density shows a peak when the gas flow rate is close to the tipping point. Furthermore, an increase of gas flow rate, and thus a lower gas outlet temperature (see Figure 7), still increases the thermal power in most cases. However, when the gas flow is increased to just above the tipping point, the thermal power slightly decreases due to a lower conversion and the accompanied strong decrease of gas outlet temperature. As the solid outlet temperature of the purely inert moving bed equals the gas inlet temperature in all cases shown, the energy density of the solid material remains unchanged. The rise in energy density can be attributed only to the reaction enthalpy and its effect on the gas and solid outlet temperatures, when comparing inert and reactive moving bed results. In case of a gas flow rate $\dot{V}_n$ of 190 L/min and a conversion of 66.9%, the thermochemical share in energy density accounts for 23% of the total energy density of the storage material.

5.3.2. Optimizing the Gas and Particle Flow Rates for High Solid Conversion

In a next step, the flow rates were optimized for high reaction extents. For different selected particle flow rates between 1 g/s and 6 g/s, the gas flow rates were varied until the highest possible conversion could be observed for each particle flow rate. The highest conversion was found for a gas flow rate just below the tipping point, comparable to the findings in Figure 6.

In Figure 9a the temperature profiles of a moving bed with conversion optimized flow rates are displayed for steady state. Figure 9b shows the corresponding conversion profile along the bed height. The figure presents only a section of the 0.7 m long simulated geometry. The temperature profiles in the excluded section ($x = 0.2$ m to $x = 0.7$ m) show a similar trend to the temperature profiles in Figure 6. A temperature plateau in the range of 931 °C to 939 °C is formed for all flow rate combinations. In general, the profiles vary only to a small extent in the section where the oxidation occurs (position 0.05 m to 0.1 m) and sensible heat is transferred from the solid to the gas flow (position 0 m to 0.1 m). The solid temperature at the outlet is not affected by this flow rate variation. Therefore, the change in achieved energy density (see Figure 10) of the Mn-Fe-oxide particles is only caused by the different extent of conversion, as illustrated in Figure 9b. The lower the flow rates, the higher the achievable conversion. This clearly demonstrates the kinetic limitation of the moving bed with Mn-Fe-oxide particles, undergoing the redox transition $(Mn_{0.75}Fe_{0.25})_3O_4$ / $(Mn_{0.75}Fe_{0.25})_2O_3$.

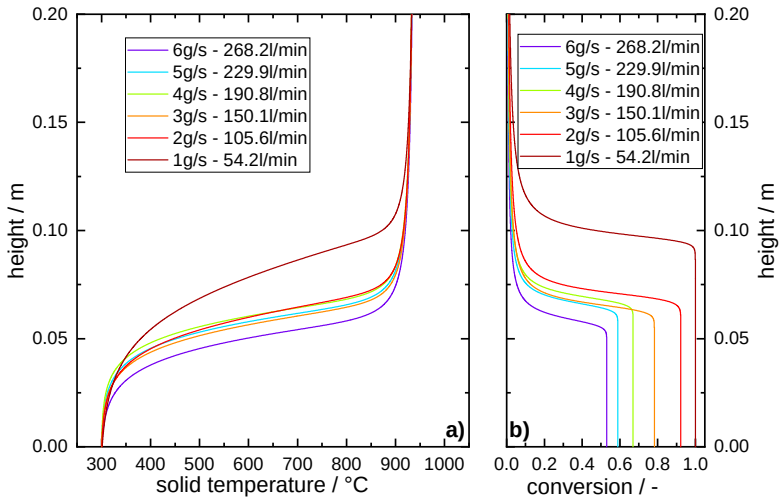

Figure 9. Solid temperatures (**a**) and conversion profiles (**b**) at a 0.2 m section of the 0.7 m simulated bed height with different particle and gas flow rates at steady state operation. The flow rates were chosen for optimized overall conversion of the particles obtained at the reactor outlet for the given particle mass flow.

The attained thermal power for the flow rate variations is plotted against the achieved energy density of the Mn-Fe-oxide particles in Figure 10. The extent of conversion and the residence time of the particles in a bed height of 10 cm are stated as well.

The energy density and the thermal power follow a contrarian trend when both flow rates are increased. Higher flow rates result in a higher thermal power, whereas the energy density of the manganese-iron oxide decreases. A higher solid mass flow leads to a decrease of residence time in the bed section exhibiting high temperature gradients. Therefore, the achievable conversion is lower, and thus, the energy density is too (see also Figure 9). As a consequence, the share of thermochemical energy in the overall energy density decreases from 30.8% with 1 g/s to 19.1% for 6 g/s. The heat capacity rate ratio F (Equation (9)) changes from 1.3 to 1.6, when the particle mass flow is increased from 1 g/s to 6 g/s. Apparently, the solid heat capacity flow together with the achievable conversion, and thus release of reaction enthalpy determines the gas flow rate at the tipping point. The heat capacity rate ratio F increases with higher gas and particle flow rates, since the achievable conversion depends on the reaction kinetics. Thus, in the case of the presented manganese-iron oxide, the position of the tipping point, i.e., solid and gas mass flows, depends also on the reaction kinetics. However, higher gas and particle flow rates still result in higher thermal power. Thus, besides the material kinetics being the limiting factor, the thermal power of the moving bed reactor can be adjusted by applying higher flow rates.

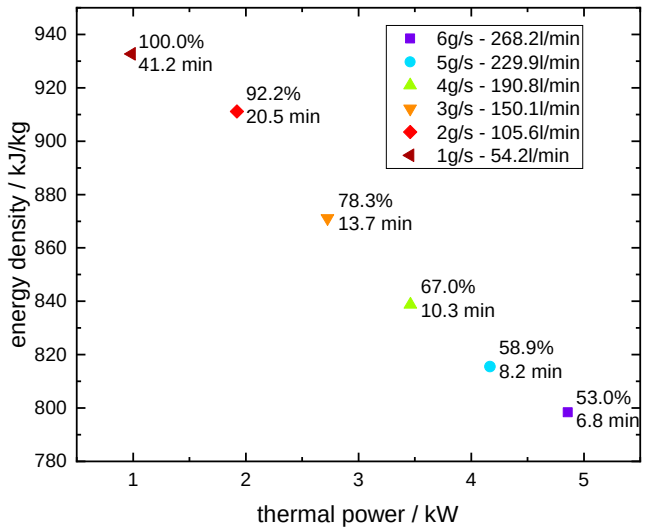

Figure 10. Thermal power of the moving bed reactor for the steady state case and energy density of the Mn-Fe-oxide with different particle flows and gas flow rates. The gas flow rates were chosen for optimized conversion of the particles at the reactor outlet. The overall conversion and the residence time of the particles in the first 10 cm after the gas inlet are also included.

So far, the following remarks can be made with respect to the simulative investigation of a moving bed with $(Mn_{0.75}Fe_{0.25})_3O_4$ / $(Mn_{0.75}Fe_{0.25})_2O_3$ particles:

- Increasing the gas flow rate has a stronger impact on the thermal power than a higher extent of conversion in the range of the operational parameters investigated.
- Reaction kinetics are the limiting factor: a material with faster kinetics would be required to allow for the exploitation of both the sensible share and the complete thermochemical share in energy density.
- The oxidation stabilizes the temperature along the bed height for a gas flow rate below the tipping point and increases the gas outlet temperature.
- The moving bed reactor facilitates a more stable gas outlet temperature with a fluctuating gas flow below the tipping point, which results from the oxidation of the Mn-Fe-oxide particles.

5.4. Sensitivity Analysis

As a next step, the effect of faster reaction kinetics and the sensitivity of the results towards a change of the convective heat transfer coefficient, e.g., due to channeling effects in the bulk material, are investigated.

5.4.1. The Influence of Channeling Effects on the Moving Bed Operation

The effect of potentially-occurring channeling on the gas-solid heat transfer and the achievable conversion was examined based on the moving bed simulation model. Furthermore, the required bed height for gas-solid heat transfer can be deduced for a bulk exhibiting channeling effects. Kunii and Suzuki [27] investigated the convective heat transfer coefficient for low Péclet numbers ($Pe < 10$) for packed bed reactors. The authors included the channeling effect in the determination of the heat transfer coefficient with a channeling ratio ζ, which is defined as the average channel length to the particle diameter d_p. Figure 11 illustrates the effect of a variation of the channeling ratio ζ on the steady state temperature and conversion profile of a moving bed with a particle mass flow of 4 g/s in counter-current to an air flow $\dot{V}_n$ of 190.8 L/min.

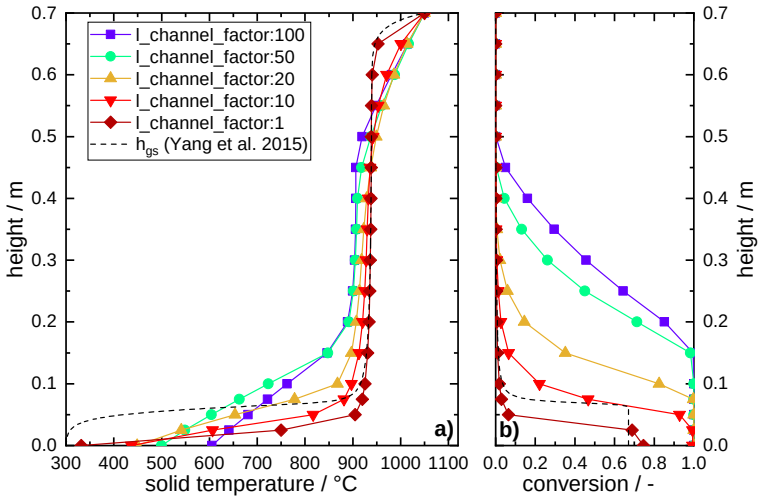

Figure 11. A variation of the channeling ratio ζ between 1 (no channels) and 100 (channels with 100 times length of d_p). (**a**) Solid temperature profile of the stationary moving bed with 4 g/s in counter-current to an air flow rate of 190.8 L/min and (**b**) the conversion profile of the Mn-Fe-oxide particles.

The channeling ratio is varied between 1 and 100, where 100 would refer to a channel length of 0.242 m. The solid temperature profile, which results from the application of the heat transfer coefficient for a moving bed (Yang et al. 2015 [22]), is added as a comparison to the channel factor of 1. The application of the heat transfer coefficient according to Kunii and Suzuki yields lower coefficients which can be identified by the lower temperature gradient at the gas inlet area. For example, the heat transfer coefficient h_{gs} equals 66.4 W/m^2/K for an application of h_{gs} according to Kunii and Suzuki, whereas h_{gs} by Yang et. al gives 182.7 W/m^2/K at a medium bed height ($x = 0.35$ m), where the solid temperature is 937 °C in both simulations.

With an increased channel length, the convective heat transfer coefficient decreases. As a result, the plateau temperature of the nearly isothermal bed height drops and the temperature gradient at the particle inlet and outlet is less steep. Therefore, the oxidation kinetics allow for an earlier beginning of the oxidation. Furthermore, the particle residence time in a temperature range, which is suitable for oxidation, is prolonged. In summary, lower convective heat transfer due to channeling effects lead to a higher extent of the reaction conversion. However, the particle outlet temperature increases, thus decreasing the sensible share in energy density. It is obvious that the convective heat transfer coefficient has a strong impact on the required bed height to assure both thermochemical and sensible heat transfer. Therefore, experimental investigations are required to analyze the flowability and potential channeling effect of manganese-iron-oxide particles in a counter-current moving bed.

5.4.2. Kinetic Limitation

In many cases, the oxidation reaction of metal oxides was found to proceed slower than the reduction and is thus often the limiting reaction step, e.g., for CuO / Cu_2O [28], Co_3O_4 / CoO [29,30], or manganese-iron-oxide [6,31]. However, some binary mixtures of Co-Cu, Cu-Mn or the pure metal oxide pair Fe_2O_3 / Fe_3O_4 promise faster oxidation kinetics [3,32]. For example, the oxidation of Fe_3O_4 was observed in less than 20 s within a temperature range of 673 K to 973 K during isothermal thermogravimetric analyses in 80% O_2, but with a conversion just above 80%.

To investigate the sensitivity of achievable energy densities and thermal power, the storage material in the current study was idealized to overcome kinetic limitations. Therefore, in this section, the kinetic limitation is assumed to be artificially inhibited by multiplying the reaction rate with the arbitrarily chosen factor of 10. In Figure 12, the kinetically improved material is compared to the actual

material concerning energy density and thermal power for fixed particle flow rates. The gas flow rate was increased to exploit the improved energy density and thus heat release transferred to the gas.

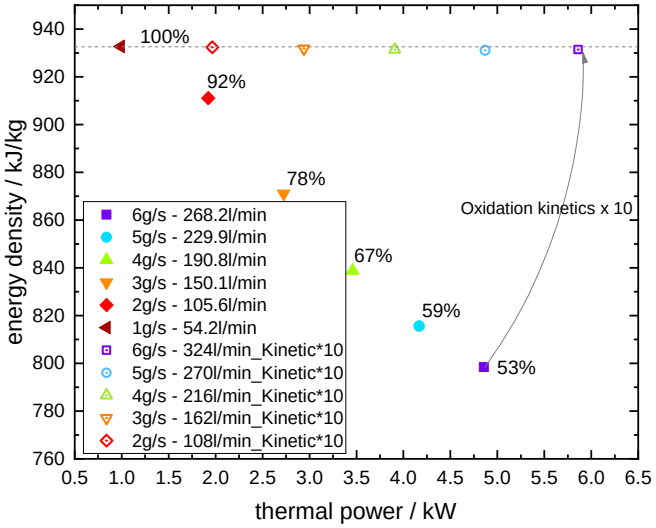

Figure 12. Energy density and thermal power of varied flow rates with either standard kinetics (full symbol) or accelerated kinetics (empty symbols). The numbers mark the conversion achieved for each simulated pair of flow rates.

The artificially accelerated kinetics (times 10) overcome the kinetic limitation. Therefore, the energy density becomes independent from the chosen flow rates or thermal power. In addition, the thermal power can be also increased because higher gas flow rates are possible. The ratio F is constant at 1.3 for the case of accelerated kinetics, which can thus be considered as the ideal flow rate ratio (tipping point) for the investigated manganese-iron oxide in the absence of the kinetic limitation.

Besides the selection of different materials with faster kinetics, other possibilities are conceivable to overcome this limitation. In principle, the application of a higher oxygen partial pressure would accelerate the kinetics [6], and thus increase the conversion for the same flow rates. However, this is technically not favored because the main advantage of the metal oxides in this system concept is to use ambient air as heat transfer fluid. Furthermore, indirect heat extraction along the bed section with nearly isothermal conditions could lead to higher reaction rates, if the plateau temperature can be lowered to below 920 °C. This could be achieved by preheating the gas indirectly along the bed section with nearly isothermal conditions before introducing the preheated gas to the moving bed. However, this would result in higher solid outlet temperatures.

6. Conclusions

A 1D moving bed simulation for thermochemical energy storage has been validated with experimental data of a packed bed reactor. The model has then been extended by particle flow for the simulation of a counter-current moving bed reactor in regard to the system concept of a solar thermal power plant. The following conclusions can be drawn for a steady state operation:

- The oxidation of the manganese-iron-oxide particles in a thermochemical moving bed leads to a bed section with nearly isothermal conditions. However, the major part of the reaction conversion does not occur in this isothermal section, but overlaps with the cooling of the particles below the temperature plateau. Thus, the thermochemical section $q_{\Delta H}$ and the sensible section q_{ox} develop simultaneously. Furthermore, the exothermic reaction leads to an increase of the energy density and thermal power in comparison to a reactor operated with inert storage material, since higher gas flows can be applied for a fixed particle flow rate. From a technical point of

view, the isothermal section would be suitable for an indirect heat transfer to lower the plateau temperature and support oxidation kinetics. Thereby, the reaction enthalpy of the storage material can be fully exploited.

- Oxidation kinetics of the redox transition $(Mn_{0.75}Fe_{0.25})_2O_3/(Mn_{0.75}Fe_{0.25})_3O_4$ are the limiting factor concerning the attainable energy density and thermal power of the moving bed reactor. A full conversion is only achievable for low gas and solid flow rate (e.g., particle flow in the range of 0.001 kg/s. If higher gas flow rates are applied and the exerted cooling effect is too high, an isothermal section cannot be formed, the conversion strongly decreases, and the temperature profile resembles the profile of a moving bed with inert storage material. Both the energy density and achievable thermal power benefit from faster kinetics when a higher reaction rate is assumed.
- The thermal power and energy density show a contrarian trend when the particle and gas flow rates are increased and the gas flow rate is determined for the maximum achievable reaction conversion. The energy density drops, whereas the thermal power is increased independently of the achieved reaction conversion for the considered operational parameters. This again shows the kinetic limitation of the chosen manganese-iron oxide.
- A sensitivity analysis showed that the potential development of channels within the moving bulk material would lower the heat transfer between solid and gas. Without consideration of channeling effects, a bed height of 20 cm would be sufficient to cool down the particle flow from 1050 °C to 300 °C with a suitable gas flow. However, if channeling effects occur, the required bed height increases up to 70 cm.

Future work will comprise an experimental investigation of the proposed reactor concept for the discharging step based on metal-oxide particles applied as thermochemical storage material and a heat transfer medium. Besides material specific parameters, such as kinetics and agglomeration, the thermal power is mainly influenced by the process control. A coupling of direct and indirect heat transfer constitutes a promising operational mode.

Author Contributions: Conceptualization, N.C.P. and M.L.; methodology, N.C.P. and I.B.; software, I.B.; validation, N.C.P., M.W. and I.B.; formal analysis, N.C.P.; investigation, N.C.P.; resources, N.C.P.; data curation, N.C.P. and M.W.; writing—original draft preparation, N.C.P.; writing—review and editing, I.B., M.W., and M.L.; visualization, N.C.P. and M.W.; supervision, M.L.; project administration, M.L.; funding acquisition, M.L. All authors have read and agreed to the published version of the manuscript.

Funding: This research received no external funding.

Acknowledgments: The authors wish to thank Henrik Winnemöller (Johannes Gutenberg University Mainz, Mainz) for proofreading. We further thank Matthias Schmidt and Kai Risthaus for intellectual discussions.

Conflicts of Interest: The authors declare no conflict of interest.

Appendix A. Specific Heat Capacity

The specific heat capacity determines the energy density for a sensible thermal energy storage material, and is thus a crucial thermophysical property for choosing a thermal energy storage material. In Figure A1, specific heat capacity data of the pure metal oxides Mn_2O_3 and Mn_3O_4 (literature data [23]) are compared to values for the mixed manganese-iron oxide measured by means of DSC.

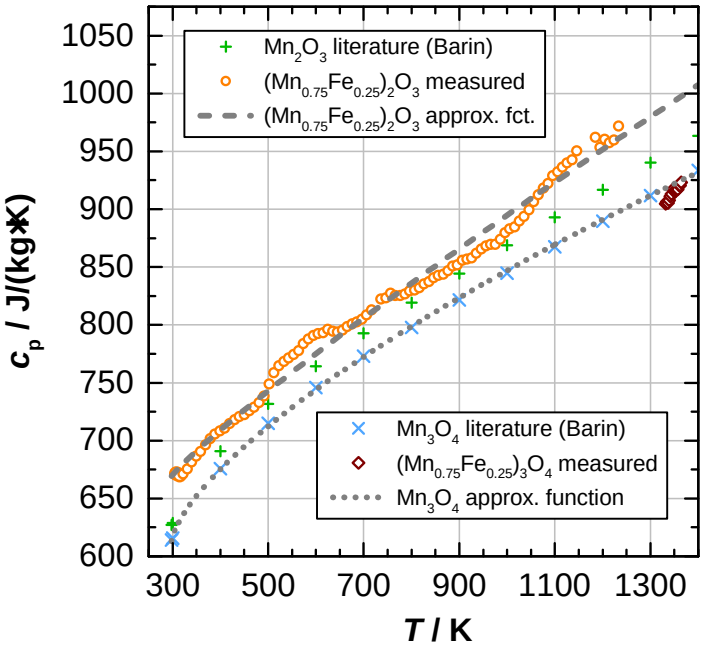

Figure A1. Specific heat capacity of manganese-iron oxide: Measured and approximated values for $(Mn_{0.75}Fe_{0.25})_2O_3$ and $(Mn_{0.75}Fe_{0.25})_3O_4$.

As the manganese-iron oxide represents a novel compound with a different lattice structure compared to iron oxide, the specific heat capacities of the mixed oxide cannot be calculated from the specific heat capacities of the respective single oxides Mn_2O_3 and Fe_2O_3 for the oxidized phase and Mn_3O_4 and Fe_3O_4 for the reduced phase of Mn-Fe-oxide, respectively. Therefore, the specific heat capacities $c_{p,ox}$ and $c_{p,red}$ of the binary oxide were measured by means of DSC. At first, the samples were prepared by pestling the granules to powder and afterward compressing the powder to pellets (85.0 mg and 91.3 mg). The compressed pellets were calcined at 950 °C for 10 h in air prior to the measurements. Finally, the pellets were heated in a Pt/Rh-crucible with a pierced lid from 30 °C up to 1200 °C with 10 K/min in an air flow of 50 mL/min (norm condition). Using a baseline measurement, a sensitivity calibration measurement with a sapphire disc of known c_p-values and the actual sample measurement, the unknown c_p-values of Mn-Fe oxide can be evaluated based on a comparative method. Between ~400 K and ~1000 K, the measured values of the oxidized phase are in the range of the pure manganese oxide Mn_2O_3. However, above ~1050 K the measured values exceed the pure metal oxide data. The curve of measured values for the oxidized phase can be best approximated with a power equation:

$$c_{p,ox}(T) = \left(669.28596 + 0.62604 \left(\frac{T}{\mathrm{K}} - 298\right)^{0.8982}\right) \mathrm{J/kg/K}. \quad \text{(A1)}$$

After a complete reduction, only a few values were obtained for the reduced phase $(Mn_{0.75}Fe_{0.25})_3O_4$. Nevertheless, they are in the range of the pure manganese oxide Mn_3O_4. The specific heat capacity of the reduced phase is approximated using the literature data for Mn_3O_4:

$$c_{p,red}(T) = \left(613.07996 + 2.58034 \left(\frac{T}{\mathrm{K}} - 298\right)^{0.68764}\right) \mathrm{J/kg/K}. \quad \text{(A2)}$$

Appendix B. Experiment for Model Validation

In the fixed-bed experiment for validation, manganese-iron-oxide particles were cooled by a gas flow of 10 L/min (norm condition). The temperatures of the gas at the inlet of the reaction bed and the

temperature of the tube furnace, which enclosed the fixed-bed reactor, were decreased by 5 K/min. In Figure A2, the gas inlet temperature and the temperatures of the bulk and the reactor tube wall, the latter measured on the outer surface of the tube, are displayed for the first 15 min of the experiment.

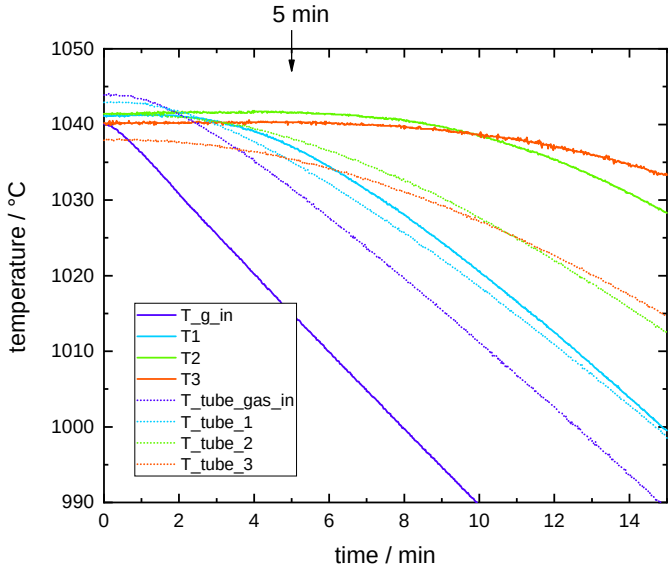

Figure A2. Temperatures of the gas, bulk material, and outer reactor tube wall during the first 15 min of the fixed-bed discharging experiment for the validation of the simulation. The position of the tube temperatures corresponds to the same height of the bulk temperature in the radial direction.

The temperatures of the reactor wall (dotted line) and the bulk temperatures (solid line) indicate a delay time until the effect of the decrease in temperature of the gas flow and tube furnace is measurable. Thus, it is assumed that the thermal mass of the reactor tube acts as a thermal buffer for the temperature decrease in the experiment during the first minutes of the experiment. However, no thermal mass is included in the simulation. For better comparison of the cooling rate of the bulk, and the temperature plateau position and length, the simulation was shifted by 5 min.

Appendix C. Initial Design of a 3 kW Moving Bed Reactor

A common way to design heat exchangers is via the NTU method (number of transfer units), where the capacity flows of solid and gas are compared [33]. For designing a heat exchanger, the characteristic numbers P_i, NTU_i, and ϑ indicate the influence of different fluid flow feed (counter-current, co-current, stirred vessel, etc.) on the exchanged power:

$$P_i = \frac{\dot{Q}}{(\dot{m}c_p)_i\,(T_{i,in} - T_{j,out})} = \frac{kA}{(\dot{m}c_p)_i}\,\frac{\Delta T_M}{(T_{i,in} - T_{j,out})}. \tag{A3}$$

Here, $\dot{Q}$ denotes the thermal power of the heat exchanger, and $P_i = NTU_i \cdot \vartheta$ the dimensionless temperature change with $\vartheta = \frac{\Delta T_M}{(T_{i,in} - T_{j,out})}$ and the logarithmic temperature difference ΔT_M based on the maximal temperature difference. The desired thermal power is set to 3 kW for initial calculations, and the heat exchanger is divided into three sections (see Figure 2b). The necessary solid and air flows are calculated according to an idealized convective heat transfer between gas and solid particles. The thermochemical section ($q_{\Delta H}$) is assumed to be isothermal at 895 °C, which is the onset temperature for the oxidation of $(Mn_{0.75}Fe_{0.25})_2O_3$, determined for a cooling rate of 10 K/min [6]. Thermogravimetric measurements of our group [6] show that the particles should stay at least 15 min in the thermochemical section in order to be fully oxidized. Furthermore, it is assumed that the reduced manganese-iron-oxide particles enter the moving bed at 1050 °C and exit the reactor at a desired

particle outlet temperature of 350 °C. An air inlet temperature of 300 °C is chosen for a calculation of an achievable air outlet temperature. The air flow is limited to air velocities below the fluidization velocity [34]. Furthermore, a temperature difference of 2 K is assumed between gas and solid, when the air flow exits the thermochemical section $q_{\Delta H}$. The necessary particle mass flow for a thermal power of 3 kW can be determined with

$$\dot{m}_s = \frac{3kW}{q_{red} + q_{\Delta H} + q_{ox}} \tag{A4}$$

to 4 g/s based on the reduced phase of manganese-iron oxide. Here, the heat transfer of each section is calculated with the specific heat capacity of Mn_2O_3 and Mn_3O_4 [23] as, e.g., $\mathrm{d}q_{red} = \int_{895\,^\circ\mathrm{C}}^{1050\,^\circ\mathrm{C}} c_{p,s}(T_s)\,\mathrm{d}T_s$. In the thermochemical section, the specific reaction enthalpy of 271 J/g based on the oxidized phase results in a heat transfer $q_{\Delta H}$. The required air flow is calculated by considering the heat transfer in the sensible section q_{ox} and thermochemical section $q_{\Delta H}$. With the assumption that the air stream leaves the thermochemical section with a temperature difference of 2 K, the supplied heat of the solid phase can be determined with $q_{ox} + q_{\Delta H}$ resulting in:

$$\dot{m}_g = \frac{\dot{Q}_{ox} + \dot{Q}_{\Delta H}}{\int_{300\,^\circ\mathrm{C}}^{893\,^\circ\mathrm{C}} c_{p,g}(T)\,\mathrm{d}T_g} = 4\,\mathrm{g/s}. \tag{A5}$$

This mass flow rate is above the minimal air flow of 0.5 g/s, which is required to provide enough oxygen for a full oxidation of 4 g/s manganese-iron-oxide particle flow. With fixed mass flow rates of gas and solid particles, the gas and solid temperatures at each border between the three sections can be calculated. In the end, a gas outlet temperature of 998 °C can be expected for the ideal case. As a result, the thermochemical share in transferred heat equals 31%.

The dimension of each section is determined with the assumption of ideal convective heat transfer according to Yang et al. [22]. For each section h_{gs} is calculated with a logarithmic temperature

$$\vartheta_m = \frac{\Delta T_{in} - \Delta T_{out}}{\ln(\frac{\Delta T_{in}}{\Delta T_{out}})} \tag{A6}$$

for inner diameters of the moving bed reactor between 10 mm and 220 mm. The convective heat transfer $Q = h_{gs} \cdot a_{gs} \cdot \Delta T$ yields the required particle surface to transfer the desired heat, and thus the reactor height h_R in relation to reactor diameter d_R and particle size d_p with $a_{gs} = \frac{3\pi d_R^2 h_R(1-\epsilon_b)}{2d_p}$. In the end, a reactor height of 700 mm and a diameter of 0.152 m for an average particle diameter of 2.5 mm were chosen to assure both sensible and thermochemical heat transfer without fluidizing the particles.

References

1. Pardo, P.; Deydier, A.; Anxionnaz-Minvielle, Z.; Rougé, S.; Cabassud, M.; Cognet, P. A review on high temperature thermochemical heat energy storage. *Renew. Sustain. Energy Rev.* **2014**, *32*, 591–610. doi:10.1016/j.rser.2013.12.014. [CrossRef]
2. Wu, S.; Zhou, C.; Doroodchi, E.; Nellore, R.; Moghtaderi, B. A review on high-temperature thermochemical energy storage based on metal oxides redox cycle. *Energy Convers. Manag.* **2018**, *168*, 421–453. doi:10.1016/j.enconman.2018.05.017. [CrossRef]
3. Block, T.; Schmücker, M. Metal oxides for thermochemical energy storage: A comparison of several metal oxide systems. *Sol. Energy* **2016**, *126*, 195–207. doi:10.1016/j.solener.2015.12.032. [CrossRef]
4. André, L.; Abanades, S.; Flamant, G. Screening of thermochemical systems based on solid-gas reversible reactions for high temperature solar thermal energy storage. *Renew. Sustain. Energy Rev.* **2016**, *64*, 703–715. doi:10.1016/j.rser.2016.06.043. [CrossRef]
5. Wokon, M.; Kohzer, A.; Linder, M. Investigations on thermochemical energy storage based on technical grade manganese-iron oxide in a lab-scale packed bed reactor. *Sol. Energy* **2017**, *153*, 200–214. doi:10.1016/j.solener.2017.05.034. [CrossRef]

6. Wokon, M.; Block, T.; Nicolai, S.; Linder, M.; Schmücker, M. Thermodynamic and kinetic investigation of a technical grade manganese-iron binary oxide for thermochemical energy storage. *Sol. Energy* **2017**, *153*, 471–485. doi:10.1016/j.solener.2017.05.045. [CrossRef]
7. Chen, C.; Lee, H.H.; Chen, W.; Chang, Y.C.; Wang, E.; Shen, C.H.; Huang, K.E. Study of an Iron-Based Oxygen Carrier on the Moving Bed Chemical Looping System. *Energy Fuels* **2018**, *32*, 3660–3667. doi:10.1021/acs.energyfuels.7b03721. [CrossRef]
8. Zeng, L.; Tong, A.; Kathe, M.; Bayham, S.; Fan, L.S. Iron oxide looping for natural gas conversion in a countercurrent moving bed reactor. *Appl. Energy* **2015**, *157*, 338–347. doi:10.1016/j.apenergy.2015.06.029. [CrossRef]
9. Tong, A.; Zeng, L.; Kathe, M.V.; Sridhar, D.; Fan, L.S. Application of the Moving-Bed Chemical Looping Process for High Methane Conversion. *Energy Fuels* **2013**, *27*, 4119–4128. doi:10.1021/ef3020475. [CrossRef]
10. Yanagiya, T.; Yagi, J.; Omori, Y. Reduction of iron oxide pellets in moving bed. *Ironmak. Steelmak.* **1979**, *6*, 93–100.
11. Takenaka, Y.; Kimura, Y. Mathematical model of direct reduction shaft furnace and its application to actual operations of a model plant. *Comput. Chem. Eng.* **1986**, *10*, 67–75. [CrossRef]
12. Parisi, D.R.; Laborde, M.A. Modeling of counter current moving bed gas-solid reactor used in direct reduction of iron ore. *Chem. Eng. J.* **2004**, *104*, 35–43. doi:10.1016/j.cej.2004.08.001. [CrossRef]
13. Ghalandari, V.; Rafsanjani, H.H. Mathematical Modeling and Simulation of Direct Reduction of Iron Ore in a Moving Bed Reactor by the Single Particle Model. *Chem. Chem. Technol.* **2019**, *13*, 205–211. doi:10.23939/chcht13.02.205. [CrossRef]
14. Negri, E.D.; Alfano, O.M.; Chiovetta, M.G. Moving-Bed Reactor Model for the Direct Reduction of Hematite. Parametric Study. *Ind. Eng. Chem. Res* **1995**, *34*, 4266–4276. doi:10.1021/ie00039a017. [CrossRef]
15. Valipour, M.S.; Saboohi, Y. Numerical investigation of nonisothermal reduction of hematite using Syngas: The shaft scale study. *Model. Simul. Mater. Sci. Eng.* **2007**, *15*, 487–507. doi:10.1088/0965-0393/15/5/008. [CrossRef]
16. Rahimi, A.; Niksiar, A. A general model for moving-bed reactors with multiple chemical reactions part I: Model formulation. *Int. J. Miner. Process.* **2013**, *124*, 58–66. doi:10.1016/j.minpro.2013.02.015. [CrossRef]
17. Kim, H.; Miller, D.C.; Modekurti, S.; Omell, B.; Bhattacharyya, D.; Zitney, S.E. Mathematical modeling of a moving bed reactor for post-combustion CO2capture. *AIChE J.* **2016**, *62*, 3899–3914. doi:10.1002/aic.15289. [CrossRef]
18. Preisner, N.C.; Block, T.; Linder, M.; Leion, H. Stabilizing Particles of Manganese-Iron Oxide with Additives for Thermochemical Energy Storage. *Energy Technol.* **2018**, *6*, 2154–2165. doi:10.1002/ente.201800211. [CrossRef]
19. Nield, D.A.; Bejan, A. *Convection in Porous Media*; Springer International Publishing: Cham, Switzerland, 2017. doi:10.1007/978-3-319-49562-0. [CrossRef]
20. Bauer, R.; Schlünder, E.U. Effective radial thermal conductivity of packings in gas flow. *Int. Chem. Eng.* **1978**, *18*, 189–204.
21. Zehner, P.; Schlünder, E.U. Einfluß der Wärmestrahlung und des Druckes auf den Wärmetransport in nicht durchströmten Schüttungen. *Chem. Ingeniuer Technol.* **1972**, *44*, 1303–1308 [CrossRef]
22. Yang, W.; Zhou, Z.; Yu, A. Particle scale studies of heat transfer in a moving bed. *Powder Technol.* **2015**, *281*, 99–111. doi:10.1016/j.powtec.2015.04.071. [CrossRef]
23. Barin, I.; Platzki, G. *Thermochemical Data of Pure Substances*, 3rd ed.; VCH Verlagsgesellschaft mbH: Weinheim, Germany, 1995. doi:10.1002/9783527619825. [CrossRef]
24. Ksiazek, M.; Manik, T.; Tangstad, M.; Ringdalen, E. The thermal diffusivity of raw materials for ferromanganese production. In Proceedings of the INFACON International Ferro-Alloys Congress, Almaty, Kazahstan, 9–12 June 2013.
25. Palacios, A.; Calderón, A.; Barreneche, C.; Bertomeu, J.; Segarra, M.; Fernández, A.I. Study on solar absorptance and thermal stability of solid particles materials used as TES at high temperature on different aging stages for CSP applications. *Sol. Energy Mater. Sol. Cells* **2019**, *201*, 110088. [CrossRef]
26. Wang, H.; Ning, X.; Wang, Q.; Liu, Y.; Song, Y. Preparation and properties of high emissivity Fe–Mn–matrix coatings by air plasma spraying. *Mater. Res. Innov.* **2015**, *19*, S29–S33. [CrossRef]
27. Kunii, D.; Suzuki, M. Particle-to-fluid heat and mass transfer in packed beds of fine particles. *Int. J. Heat Mass Transf.* **1967**, *10*, 845–852. doi:10.1016/0017-9310(67)90064-6. [CrossRef]

28. Wu, S.; Zhou, C.; Doroodchi, E.; Moghtaderi, B. A unique phase change redox cycle using CuO/Cu2O for utility-scale energy storage. *Energy Convers. Manag.* **2019**, *188*, 366–380. doi:10.1016/j.enconman.2019.03.055. [CrossRef]
29. Schrader, A.J.; Muroyama, A.P.; Loutzenhiser, P.G. Solar electricity via an Air Brayton cycle with an integrated two-step thermochemical cycle for heat storage based on Co_3O_4/CoO redox reactions: Thermodynamic analysis. *Sol. Energy* **2015**, *118*, 485–495. doi:10.1016/j.solener.2015.05.045. [CrossRef]
30. Muroyama, A.P.; Schrader, A.J.; Loutzenhiser, P.G. Solar electricity via an Air Brayton cycle with an integrated two-step thermochemical cycle for heat storage based on Co3O4/CoO redox reactions II: Kinetic analyses. *Sol. Energy* **2015**, *122*, 409–418. doi:10.1016/j.solener.2015.08.038. [CrossRef]
31. Carrillo, A.J.; Serrano, D.P.; Pizarro, P.; Coronado, J.M. Understanding Redox Kinetics of Iron-Doped Manganese Oxides for High Temperature Thermochemical Energy Storage. *J. Phys. Chem. C* **2016**, *120*, 27800–27812. doi:10.1021/acs.jpcc.6b08708. [CrossRef]
32. Bush, H.E.; Loutzenhiser, P.G. Solar electricity via an Air Brayton cycle with an integrated two-step thermochemical cycle for heat storage based on Fe_2O_3/Fe_3O_4 redox reactions: Thermodynamic and kinetic analyses. *Sol. Energy* **2018**, *174*, 617–627. doi:10.1016/j.solener.2018.09.043. [CrossRef]
33. *VDI-Wärmeatlas*; Springer: Berlin/Heidelberg, Germany, 2013. doi:10.1007/978-3-642-19981-3. [CrossRef]
34. Wen, C.Y.; Yu, Y.H. A Generalized Method for Predicting the Minimum Fluidization Velocity. *AIChE J.* **1966**, *12*, 610–612. [CrossRef]